Comparison between PIV measurements and computations of the near-wake of an actuator disc

2014 J. Phys.: Conf. Ser. 524 012173

(http://iopscience.iop.org/1742-6596/524/1/012173)

Comparison between PIV measurements and computations of the near-wake of an actuator disc.

S. J. Andersen[1a], L. E. M. Lignarolo[2a], D. Ragni[2], C. J. Simão Ferreira[2], J. N. Sørensen[1], R. F. Mikkelsen[1], G. J. W. van Bussel[2]

[1] Department of Wind Energy, Building 403, Technical University of Denmark, DK-2800 Lyngby, Denmark

[2] Faculty of Aerospace Engineering, Delft University of Technology, 2600 AA Delft, The Netherlands

E-mail: [1a]: sjan@dtu.dk, [2a]: L.E.M.Lignarolo-2@tudelft.nl

Abstract. Experimental stereoscopic PIV measurements in the wake of a two-bladed rotor and a porous actuator disc are compared to numerical simulation of an actuator disc. Compared to previous literature, the focus of the present analysis is on the near wake, where the actuator discs fail to represent the complex flow structures correctly, which affects the downstream representation of the full wake behind a real rotor. The near wake region is characterised by the instability and breakdown of the tip-vortex helical system, which constitutes the onset of a stronger mixing process. The comparison focuses on the turbulent structures in the shear layer at the borders of the wake through the analysis of the Reynolds stresses and by employing POD on two separate regions. The analysis shows that the actuator discs fail to capture the details of the complex flow behind a rotor, but that the experimental and numerical actuator discs are generally comparable at a certain distance behind the actuator disc. This project is intended to provide the basis for understanding the origin of the limitations of the current wake models based on the actuator disc assumption.

1. Introduction

A common approach to the numerical simulation of wind farms is to model the rotors as actuator discs. However, this approach disregards the effects of significant flow structures in the near-wake, e.g. the helical instability of the tip vortices, with repercussions in the whole wake mixing process as a consequence. Some researchers have performed experimental comparisons between scaled wind turbine rotors and porous discs, e.g. Aubrun et al. 2013 [1]. The aim of the present work is to show similarities and differences between the numerical actuator disc model and its experimental representation through a porous disc as well as an experimental two-bladed rotor. The experiments are conducted with high resolution stereoscopic particle image velocimetry(PIV) in the Open Jet Facility(OJF) wind tunnel at TUDelft. The actuator disc is reproduced with a porous disc composed by several layers of metallic mesh. The device matches the diameter and drag coefficient of a two-bladed wind turbine model with a $0.60m$ diameter, whose analysis has been conducted in previous works, see Lignarolo et al. [2]. The CFD code used for the actuator disc simulation is EllipSys3D developed by Michelsen [3] and Sørensen [4]. The wake velocity, Reynolds stresses, and wake expansion will be compared for the two numerical models and the experiments. The turbulent structures in the shear layer are

examined by employing POD on the LES and PIV fields. The comparison between experimental and numerical data will examine the limitations and potentialities of the physical representation of an actuator disc, both experimentally and numerically, which in turn will lead to further insights about the limitation of the actuator disc assumption when compared to an actual rotor and applied for wind farms with small turbine spacing.

2. Methodology

2.1. Experimental Setup

Experiments have been conducted in the low-speed closed-loop open-jet wind tunnel located at the Aerodynamics Department of the Delft University of Technology. The wind tunnel, with its octagonal test section has an equivalent diameter of $3m$ and a contraction ratio of $3:1$, delivering a uniform flow with approximately 0.5% turbulent intensity up to $1m$ from the nozzle and lower than 2% at $6m$ from the nozzle exit. A two-bladed horizontal axis wind turbine with a $0.6m$ diameter has been designed for an optimal tip-speed ratio $\lambda = \frac{\omega r}{U_\infty} = 6$. A detailed characterization of the wind tunnel flow field and more information on the wind turbine design can be found in Lignarolo et al. [2]. For the present experiments, the freestream wind velocity is $U_\infty = 4.7m/s$ and the rotational speed is $\omega = 109.3rad/s$, which gives $\lambda = 6.97$. With these conditions the maximum chord-based Reynolds number is $Re_{ct} = 96,000$. A $0.6m$ diameter porous disc is built by superimposing different layers of metal mesh, similarly to Aubrun et al. [5] and Aubrun et al. [1]. In order to obtain the same wake expansion, the wind turbine and the porous disc must have the same axial force, i.e. thrust coefficient C_T. This is achieved with three layers of metal mesh and a final porosity $p = 32\%$. Table 2.1 summarises all the information about the experimental conditions.

Table 1. Wake expansion factors for infinite row of turbines.

Parameters	WT	AD
Freestream velocity, U_∞	$4.7m/s$	$4.7m/s$
Rotational frequency, ω	$109.3rad/s$	–
Reynolds (chord based) blade root, $r/R = 0.20$, Re_{cr}	$32,000$	–
Reynolds (chord based) blade tip, $r/R = 1.0$, Re_{ct}	$96,000$	–
Reynolds (diameter based), Re_C	$188,000$	$188,000$
Tip-speed ratio, λ	6.97	–

Stereoscopic PIV experiments are conducted to obtain the three component velocity fields in the rotor wake. A stereoscopic PIV setup has been installed on a traversing system able to scan the flow field in the wake of the horizontal axis wind turbine wake. The required illumination is provided by a Quantel Evergreen Nd:YAG laser system with an average output of $200mJ/pulse$. Two LaVision Imager Pro LX 16 Mpix ($4870 \times 3246px^2, 12bits$) with pixel pitch of $7.4\mu m/px$ are used to acquire images with a field of view of $0.297 \times 0.227m^2 (0.50 \times 0.39diameters)$. The entire setup was mounted on a traversing system able to translate in 2D of about $1.2m \times 0.9m$. Series of unconditioned double frame recordings have been acquired and processed by LaVision Davis 8.1.4 and further combined to form a total flow field as shown in Sections 3.1 and 3.2. Ensembles of 200 random PIV samples per field of view are averaged in order to obtain time-average three-component velocity fields and turbulence statistics: 1000 samples are acquired in two specific locations where the POD analysis is performed. Interrogation windows of $24 \times 24px^2$ with 50% overlap allows to have a resolution element of $1.46mm$, and a vector spacing of $0.732mm$.

2.2. Computational Fluid Dynamics

A Computational Fluid Dynamic(CFD) simulation was performed using the 3D flow solver, EllipSys3D, which was developed by Michelsen [3] and Sørensen [4]. EllipSys3D solves the discretised, incompressible Navier-Stokes equations in general curvilinear coordinates using a block structured finite volume approach.

The turbulent closure is attained through Large Eddy Simulation(LES), where the larger eddies are resolved explicitly on the grid and eddies smaller than the spatial filter is modeled by a sub-grid scale(SGS) model. The employed SGS model is based on the mixed scale model by Ta Phuoc et al. [6].

The flow field is thus approximated by solving the filtered 3D incompressible Navier-Stokes equations for $\overline{\mathbf{V}}$:

$$\frac{\partial \overline{\mathbf{V}}}{\partial t} + \overline{\mathbf{V}} \cdot \nabla \overline{\mathbf{V}} = -\frac{1}{\rho}\nabla \overline{p} + \nabla[(\nu + \nu_{SGS})\nabla \overline{\mathbf{V}}] + \frac{1}{\rho}\mathbf{f}_{WT} + \frac{1}{\rho}\mathbf{f}_{turb}. \tag{1}$$

$$\nabla \overline{\mathbf{V}} = 0. \tag{2}$$

where ρ denotes density, p is pressure, and ν is eddy viscosity. Actuators or body forces($\mathbf{f}_{WT}$ and $\mathbf{f}_{turb}$) are explicitly applied in the simulations to model the effect of the wind turbine and turbulence. The pressure correction is solved using the PISO algorithm and pressure decoupling is achieved using the Rhie/Chow interpolation technique. The convective terms are discretised as a combination of the third order QUICK scheme and the fourth order CDS scheme.

The actuator disc(AD) method is a well-known approach for modeling wind turbines and the description here is kept very concise, see Mikkelsen [7] for more extensive details. The AD is modeled by imposing body forces($\mathbf{f}_{WT}$) over the entire rotor area in the flow. The forces are distributed constantly across the actuator disc to give $C_T = 0.93$ as for the experiments, but smeared numerically perpendicular to the AD to avoid singular behaviour.

The mesh is $20R \times 20R \times 20R$ with a uniform distribution in the central region($\pm 2.5R$) around the actuator disc. The resolution is 31 cells per radius, which is rather fine for full 3D LES simulations as actuator discs are often resolved using $10 - 20$ cells per radius. In the following, X denotes the streamwise, Y the vertical, and Z the lateral direction normalised by the rotor/disc radius. The corresponding velocity components are U, V, and W, respectively.

2.3. Proper Orthogonal Decomposition

Proper Orthogonal Decomposition(POD) is a statistical method, which yields an optimal linear subspace, optimal in terms of the variance, i.e. the energy content when performed on the velocity fluctuations. The resulting POD modes are sorted in terms of energy. POD was first introduced as an analysis tool for detecting large coherent turbulent structures by Lumley [8]. POD is briefly outlined in the following, but for further details reference is made to the seminal work by Sirovich [9], Aubry et al. [10], or the general overview given by Berkooz et al. [11].

The normalised velocity components ($\mathbf{u} = (U, V, W)$) of each of the N extracted slices are organised in vectors $\mathbf{u_i}$, which constitute a matrix with the velocity fluctuations defined as:

$$\mathbf{U} = [\mathbf{u'_1} \dots \mathbf{u'_N}] \tag{3}$$

It is common practice to subtract the mean value $\mathbf{u_0}$, because it essentially reduces the number of dimensions by one by considering the velocity fluctuations, which results in optimising the energy content of the resulting POD modes. Therefore, $\mathbf{u'_j}$ is defined as:

$$\mathbf{u'_j} = \mathbf{u_j} - \frac{1}{N}\sum_{i=1}^{N} \mathbf{u_i} = \mathbf{u_j} - \mathbf{u_0} \tag{4}$$

The decomposition is then based on the hermetian symmetric two-point velocity correlation tensor of $N \times N$ given as:

$$\mathbf{R} = \mathbf{U^T U} \tag{5}$$

Defining an eigenvalue matrix with $\lambda_1 \geq \lambda_2 \geq \ldots \lambda_{N-1} > 0$:

$$\mathbf{\Lambda} = \begin{pmatrix} \lambda_1 & & \mathbf{0} \\ & \ddots & \\ \mathbf{0} & & \lambda_{N-1} \end{pmatrix}$$

and matrix of orthonormal eigenvectors:

$$\mathbf{G} = [\mathbf{g_1} \ldots \mathbf{g_{N-1}}] \tag{6}$$

yields an eigenvalue problem of the Fredholm type:

$$\mathbf{RG} = \mathbf{G\Lambda} \tag{7}$$

The basis vectors or POD modes can be written as:

$$\phi_k = \frac{\mathbf{Ug_j}}{\|\mathbf{Ug_j}\|} \tag{8}$$

These are spatial modes, which contain information on the coherent structures. POD can be considered an energy filter, which reveal the large spatial turbulent structures.

3. Results

The numerical AD simulation has been conducted with the same C_T as experimentally measured. Subsequently, the results behind the experimental and the simulated AD have been compared in order to examine the wake velocities and the Reynolds stresses in the near wake. The turbulent structures in the shear layer are examined using POD.

3.1. Wake Velocity Profiles

The averaged streamwise velocity profiles at three different positions are compared for the experimental and numerical results in Figure 1. The numerical results yield a higher wake velocity for all downstream distances, although the three profiles are very comparable for $X = 2R$. The difference between the three profiles increase further from the rotor/disc, and particular in the root region, where there is a large deficit behind the rotor.

The spatial average of the axial and vertical velocity components are shown in Figure 2, where the velocity components are normalised by the freestream axial velocity. Here it is also clear how the wake velocity behind the numerical AD is higher than the experimental wake velocities, despite having the same C_T. The experimentally averaged velocity plots includes various streaks stemming from the root/nacelle and the structural support of the actuator disc as well as the porosity of the actuator disc, which introduce additional turbulence in the wake, which is absent in the numerical simulations. It is noteworthy how the vortex sheet appear to originate slightly below the edge of the numerical AD, i.e. $Y < 1R$, and that the wake expansion appears smaller. This is due to the numerical smearing of the forces. The vertical velocities are also comparable as they all show a large increase around the tip region, while there is only minor or no vertical velocity components in the wake behind the two actuator discs. There is no lateral velocities(not shown) behind the actuator discs, since there is no rotation as in the wake of the two-bladed rotor.

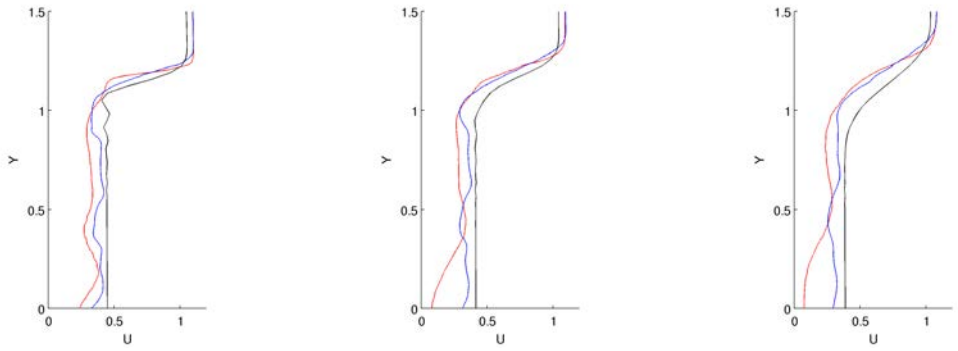

(a) $X = 2R$. (b) $X = 3R$. (c) $X = 4R$.

Figure 1. Comparison of streamwise velocity profiles behind a two-bladed rotor and an experimental and numerical actuator disc. —— : Two-bladed Turbine(exp.). —— : Actuator Disc(exp.). —— : Actuator Disc(numerical).

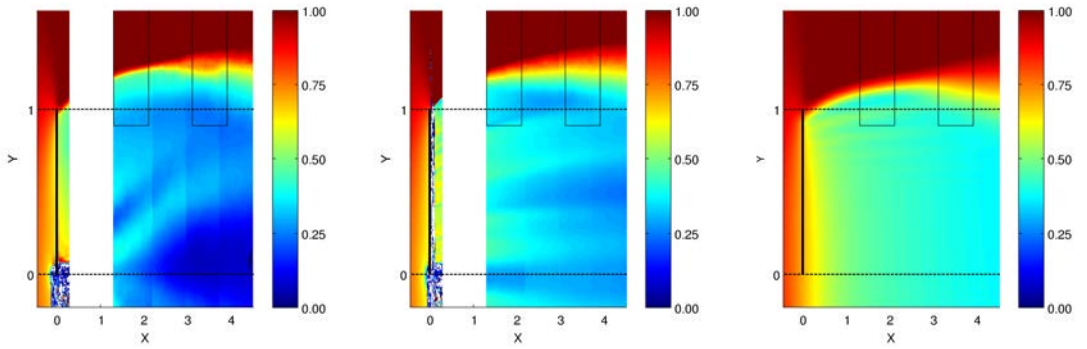

(a) Axial velocity for two-bladed rotor. (b) Axial velocity for AD(exp.). (c) xial velocity for AD(CFD).

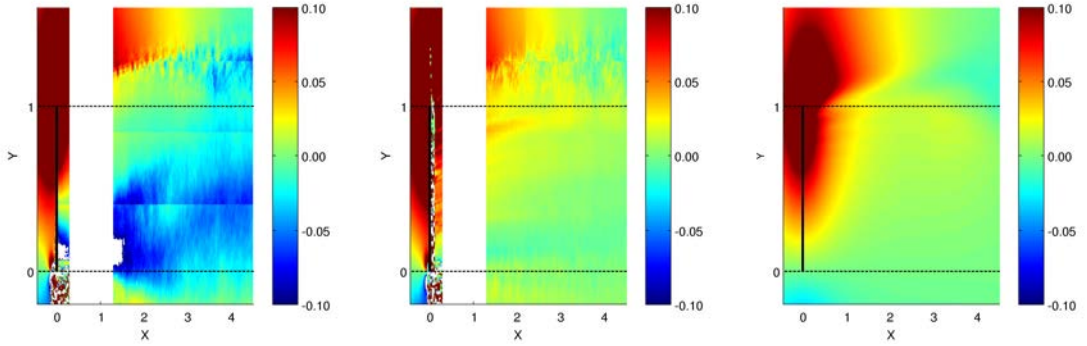

(d) Vertical velocity for two-bladed rotor. (e) Vertical velocity for AD(exp.). (f) Vertical velocity for AD(CFD).

Figure 2. Normalised average velocity components for the two-bladed rotor, AD(exp.) and AD(CFD). Full lines indicate rotor/disc and broken lines the root and tip, i.e. $Y = 0R$ and $Y = 1R$.

3.2. Reynolds Stresses

Four of the normalised Reynolds stresses in the wake behind the two actuator discs as well as behind the rotor are presented in Figures 3. The velocity fluctuations have been normalised by the freestream axial velocity, i.e. $\tau_{ij} = \overline{\frac{u_i'}{U_\infty}\frac{u_j'}{U_\infty}}$. The absence of the lateral velocity component clearly influence the Reynolds stresses in the wake behind the actuator discs. However, both actuator discs capture Reynolds stresses along the shear layer, although the magnitude is significantly smaller, because there are no concentrated tip vortices, but rather vorticity sheets stemming from the rim of the actuator discs. Furthermore, the effect of low numerical resolution(compared to the highly resolved PIV measurements) is clearly visible in the Reynolds stresses as the shear layer is both smeared and only appears after some distance downstream the actuator disc. τ_{xy} is different for the three cases in the very near wake, both in terms of distribution and level. However, the difference disappears further downstream, so τ_{xy} becomes comparable behind the experimental and numerical actuator disc from approximately $3R$ downstream. This is an important parameter for comparing the experimental and numerical actuator disc, because τ_{xy} governs the turbulunt mixing across the shear layer.

3.3. Proper Orthogonal Decomposition of the shear layer

POD is employed on data extracted in the shear layer in two different areas, one in the near wake and one in the intermediate wake. The two areas are marked by boxes in Figure 2. A total of $1,000$ instanteneous observations have been used. Figure 4 shows the first 10 sorted and 50 cummulated POD coefficients for both the near and intermediate shear layer. Comparing the POD coefficients for the two experiments clearly reveal that the turbulent structures are much more coherent in the shear layer behind an actual rotor compared to behind an actuator disc as the energy is concentrated on much fewer POD modes. The coherent structures are obviously the tip vortices in the shear layer. The absence of distinct tip vortices behind a porous actuator disc, which introduce additional turbulence into the wake, results in a much more uniform energy distribution. The opposite is the case behind the numerical actuator disc, where the most energetic POD modes contain relative more energy than the most energetic POD modes behind a two-bladed rotor. Note, that this is scaled to the total amount of turbulent kinetic energy in the flow and as seen in the Reynolds stresses the numerical simulations underestimate the total energy in the flow. This is related to the grid resolution, where the finer scales are not captured by the grid resolution, but modeled through LES, so more energy is lumped onto bigger turbulent structures. Similar trends are seen for the POD coefficients in the intermediate wake, although the energy content of the first POD modes are decreased due to turbulent diffusion.

Figures 5 depicts the first five spatial POD modes in the near wake for the three cases. The tip vortices are clearly captured behind the two-bladed rotor in the near wake. The POD modes reveal very distinct pairs on both sides of the shear layer for the first four modes, which indicates the vorticity of the tip vortices. Orthogonal mode pairing between the first and second, third and fourth POD modes are obvious. The size of the coherent structures decrease for higher POD modes as the energy content decrease. Large coherent structures are also present in the shear layer behind the actuator discs, although the structures are larger and less periodic compared to the tip vortices behind the two-bladed rotor. The structures are mainly alternating in the streamwise direction behind the experimental actuator disc as the vorticity is concentrated in a vortex sheet as opposed to the helical tip vortices originating from the rotating blades. The POD modes also reveal how the location of the shear layer is different in the experiments and the simulation as there is less wake expansion in the numerical simulation due to the numerical smearing.

Figure 6 shows the first five POD modes in the intermediate wake. Similar trends emerge, although the turbulent structures are bigger for all three cases. Interestingly, the POD modes behind the experimental and numerical actuator discs are generally comparable, particularly for

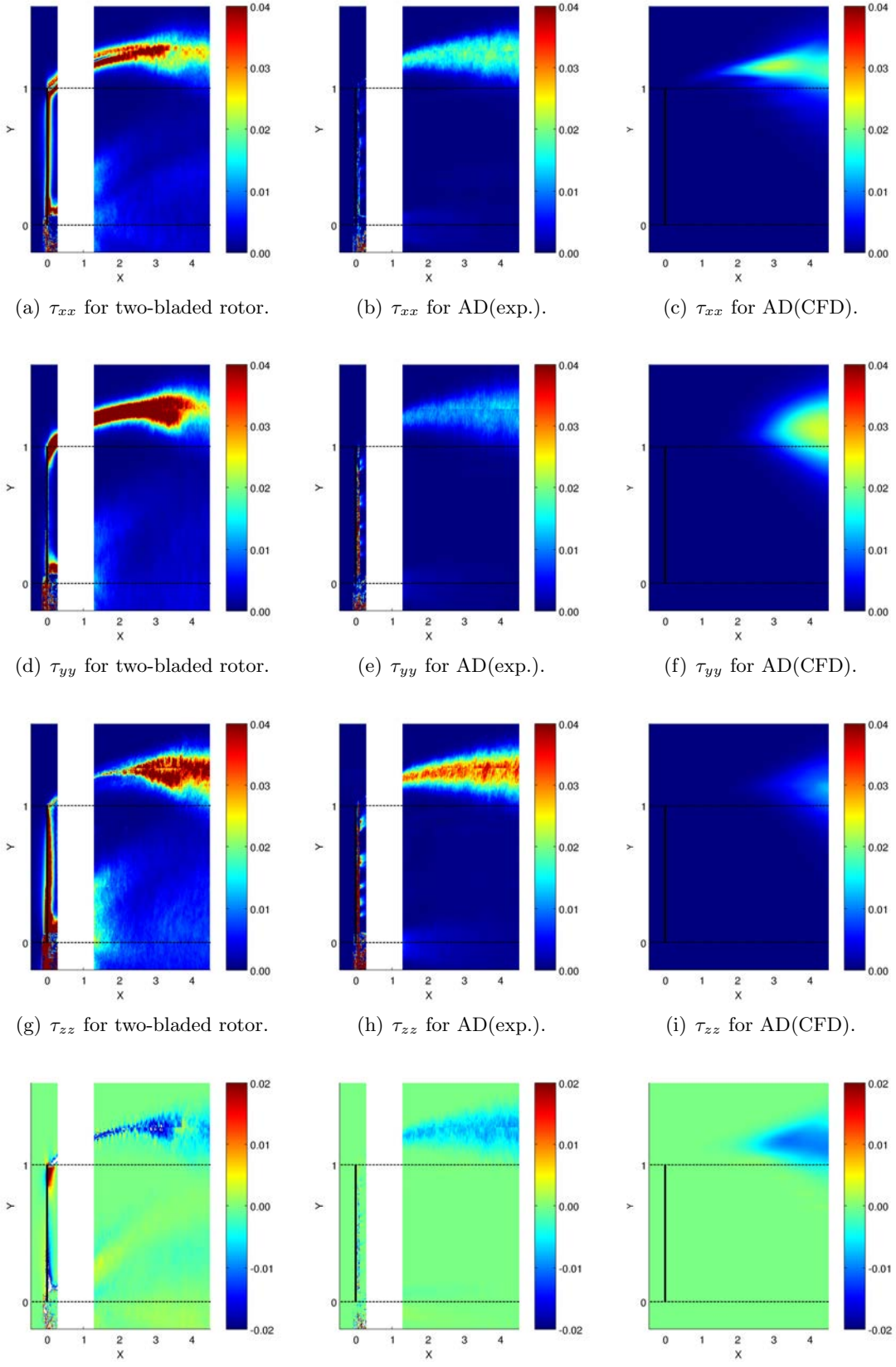

(a) τ_{xx} for two-bladed rotor. (b) τ_{xx} for AD(exp.). (c) τ_{xx} for AD(CFD).

(d) τ_{yy} for two-bladed rotor. (e) τ_{yy} for AD(exp.). (f) τ_{yy} for AD(CFD).

(g) τ_{zz} for two-bladed rotor. (h) τ_{zz} for AD(exp.). (i) τ_{zz} for AD(CFD).

(j) τ_{xy} for two-bladed rotor. (k) τ_{xy} for AD(exp.). (l) τ_{xy} for AD(CFD).

Figure 3. Normalised Reynolds stresses in the wake behind the two-bladed rotor, AD(exp.) and AD(CFD). Full lines indicate rotor/disc and broken lines the root and tip, i.e. $Y = 0R$ and $Y = 1R$.

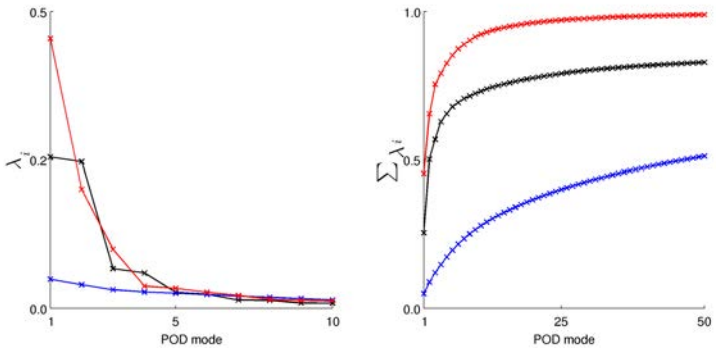

(a) Sorted POD coefficients for near wake.

(b) Cummulated POD coefficients for near wake.

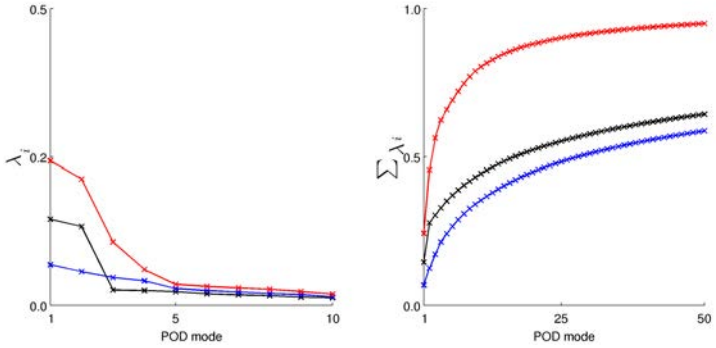

(c) Sorted POD coefficients for intermediate wake.

(d) Cummulated POD coefficients for intermediate wake.

Figure 4. Sorted and cummulated POD coefficients. —— : Two-bladed rotor. —— : Actuator disc(exp.). —— : Actuator disc(CFD).

POD mode 4 and 5, both in extent and location. So the difference in location of the shear layer seen in the near wake appears to diminsh further downstream as the experimental and numerical actuator discs compare well. This also indicates that the numerical grid resolution is sufficient as the resolved turbulent structures are comparable in size to those behind the experimental actuator disc.

4. Discussion and Conclusion

Experimental measurements in the near wake behind a two-bladed rotor and a porous actuator disc made up of different layers of metal mesh have been compared to numerical LES simulation of an actuator disc with the same, constant thrust coefficient. The comparison showed a higher axial velocity behind the numerical AD, but comparable vertical velocities around the tip/edge of the rotor and actuator discs. The Reynolds stresses in the shear layer were significantly smaller behind both actuator discs compared to the two-bladed rotor, but comparable behind the two actuator discs.

POD was performed on two areas along the shear layer, which revealed the highest relative energy content of the first POD modes in the numerical simulations followed by measurements behind the rotor, whereas the turbulent kinetic energy content of the POD modes behind the experimental AD was more evenly distributed. The spatial POD modes displayed insights into the turbulent flow structures in the shear layer, which were comparable for the two actuator

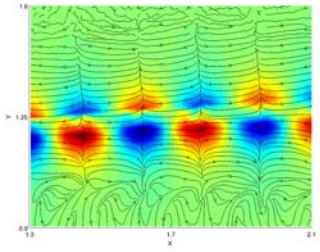

(a) POD mode 1 for two-bladed rotor.

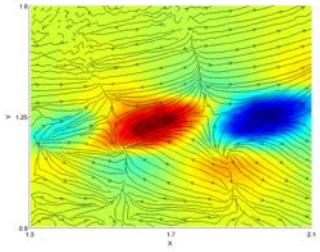

(b) POD mode 1 for AD(exp.).

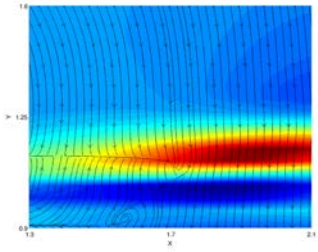

(c) POD mode 1 for AD(CFD).

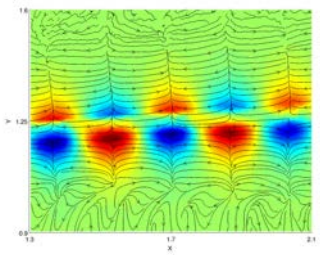

(d) POD mode 2 for two-bladed rotor.

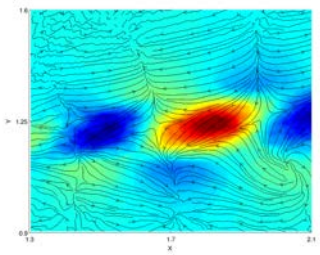

(e) POD mode 2 for AD(exp.).

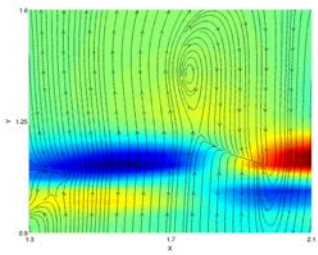

(f) POD mode 2 for AD(CFD).

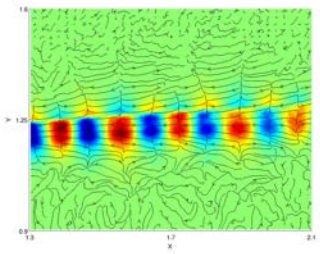

(g) POD mode 3 for two-bladed rotor.

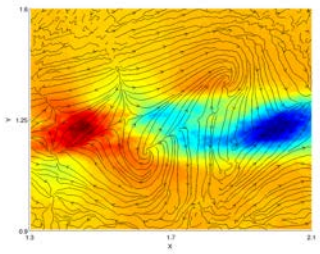

(h) POD mode 3 for AD(exp.).

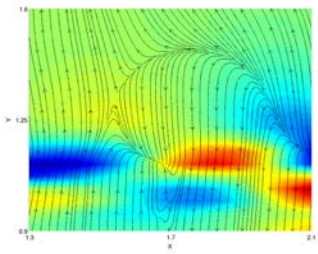

(i) POD mode 3 for AD(CFD).

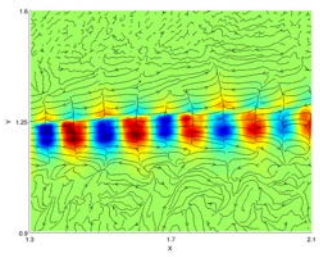

(j) POD mode 4 for two-bladed rotor.

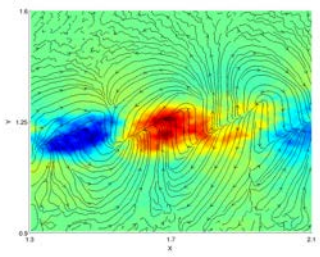

(k) POD mode 4 for AD(exp.).

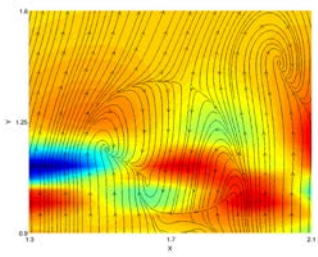

(l) POD mode 4 for AD(CFD).

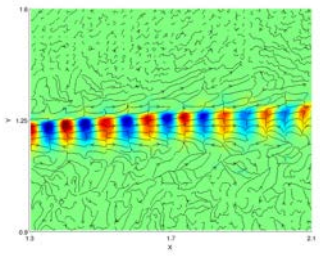

(m) POD mode 5 for two-bladed rotor.

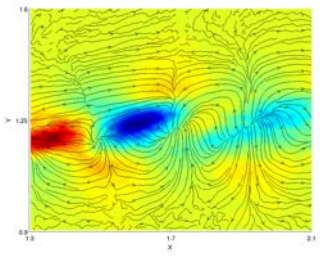

(n) POD mode 5 for AD(exp.).

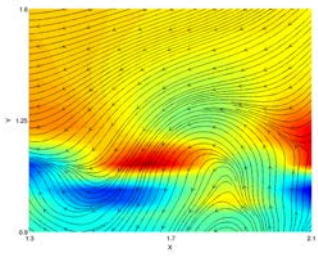

(o) POD mode 5 for AD(CFD).

Figure 5. Spatial POD modes 1-5 in the near wake for two-bladed rotor, AD(exp.) and AD(CFD).

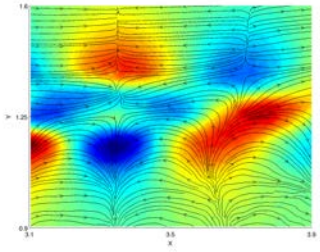

(a) POD mode 1 for two-bladed rotor.

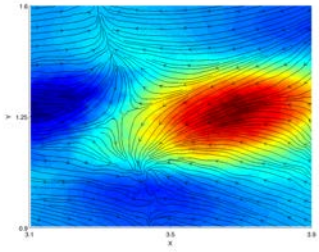

(b) POD mode 1 for AD(exp.).

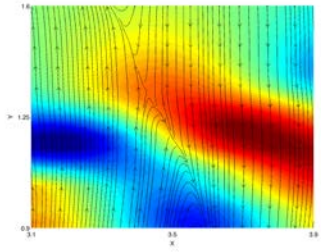

(c) POD mode 1 for AD(CFD).

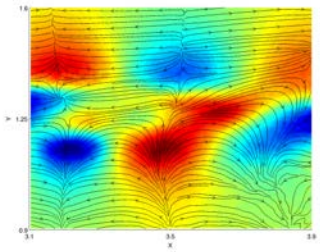

(d) POD mode 2 for two-bladed rotor.

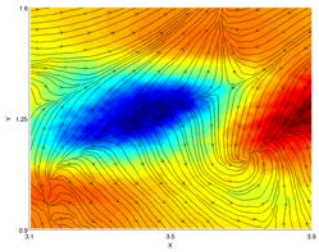

(e) POD mode 2 for AD(exp.).

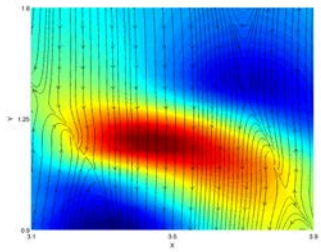

(f) POD mode 2 for AD(CFD).

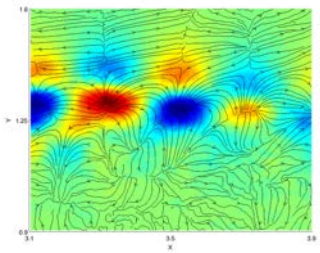

(g) POD mode 3 for two-bladed rotor.

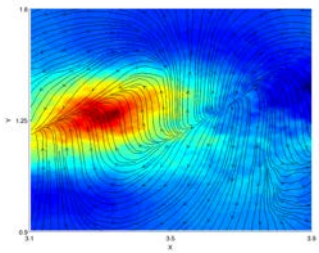

(h) POD mode 3 for AD(exp.).

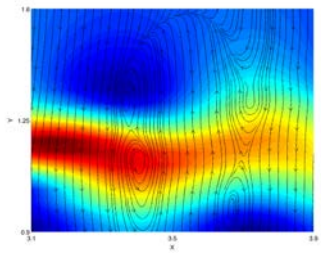

(i) POD mode 3 for AD(CFD).

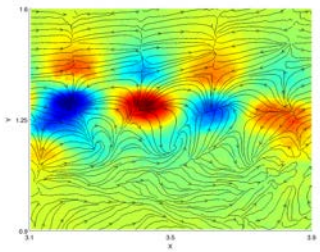

(j) POD mode 4 for two-bladed rotor.

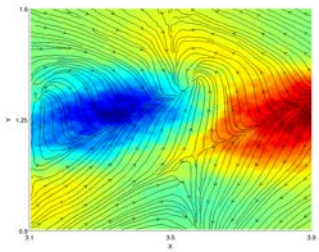

(k) POD mode 4 for AD(exp.).

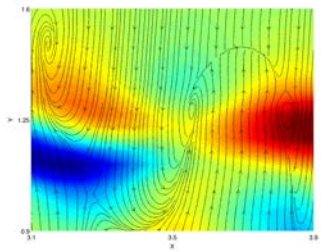

(l) POD mode 4 for AD(CFD).

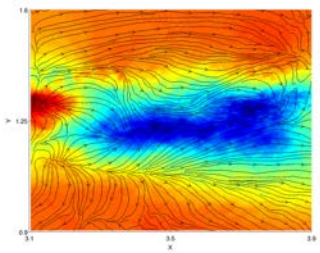

(m) POD mode 5 for two-bladed rotor.

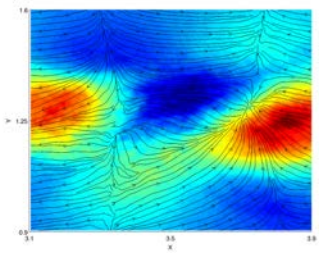

(n) POD mode 5 for AD(exp.).

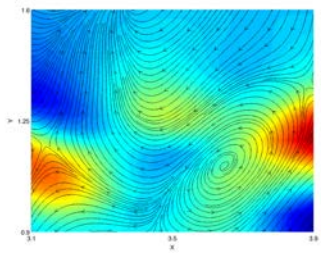

(o) POD mode 5 for AD(CFD).

Figure 6. Spatial POD modes 1-5 in the intermediate wake for two-bladed rotor, AD(exp.) and AD(CFD).

discs in the intermediate wake.

The comparison highlights difficulties involved with capturing and modeling the turbulent structures in the shear layer behind a two-bladed turbine through the use of actuator discs, experimental as well as numerical. This was shown both in terms of Reynolds stresses and by employing POD to detect the large coherent structures. However, the comparison showed that the experimental and numerical actuator discs are comparable for a number of parameters a certain distance outside the immediate near wake, although the porosity of the experimental disc introduce additional turbulence in the wake compared to the numerical representation. Having an adequate and comparable representation of the near wake behind a rotor using actuator discs is important when applying the actuator disc concept to wind farms with very low turbine spacings.

References

[1] Aubrun S, Loyer S, Hancock P and Hayden P 2013 *Journal of Wind Engineering and Industrial Aerodynamics* **120**
[2] Lignarolo L, Ragni D, Krishnaswami C, Chen Q, Ferreira C S and van Bussel G 2014 *Renewable Energy*
[3] Michelsen J A 1992 *Report AFM*
[4] Sørensen N N 1995 *General Purpose Flow Solver Applied to Flow over Hills* Ph.D. thesis Technical University of Denmark
[5] Aubrun S, Devinant P and Espana G 2007 Physical modelling of the far wake from wind turbines. application to wind turbine interactions
[6] Ta Phuoc L, Lardat R, Coutanceau M and Pineau G 1994 Rechereche et analyse de modeles de turbulence de sous maille adaptes aux ecoulements instationnaires decolles.
[7] Mikkelsen R 2003 *Actuator Disc Methods Applied to Wind Turbines* Ph.D. thesis Technical University of Denmark, Mek dept
[8] Lumley J L 1967 The structure of inhomogeneous turbulence
[9] Sirovich L 1987 *Quarterly of Appl. Math.* **XLV** 583–590
[10] Aubry N, Holmes P, Lumley J L and Stone E 1988 *J. Fluid Mech.* **192**
[11] Berkooz G, Holmes P and Lumley J L 1993 *Annual Rev. Fluid Mech* 539–575